Airfoil optimization for rotors operating in the ultra-low Reynolds number regime

Accepted to Phys. Fluids 10.1063/5.0166170

Airfoil Optimization for Rotors Operating in the Ultra-Low Reynolds Number Regime

M. Carreño Ruiz,[1] L. Renzulli,[1] and D. D'Ambrosio[1]
Department of Mechanical and Aerospace Engineering, Politecnico di Torino, Torino, 10129, Italy

(*Electronic mail: manuel.carreno@polito.it)

(Dated: 21 August 2023)

Ultra-low Reynolds number aerodynamics has gained significant attention in recent times, primarily due to the proliferation of Micro Aerial Vehicles (MAVs) and their utilization in low-density environments such as the Martian atmosphere and high altitudes in Earth's atmosphere. The Martian atmosphere presents a unique combination of low Reynolds numbers and high subsonic Mach numbers, necessitating the use of unconventional airfoil designs in this regime. This study focuses on optimizing airfoils for rotors operating in the compressible ultra-low Reynolds number regime. We demonstrate the capability of XFOIL, a panel method code incorporating an integral boundary layer formulation, to accurately predict airfoil loads when the flow remains attached. We determine the optimal camber and maximum camber positions by analyzing the four digits, two percent thickness, National Advisory Committee for Aeronautics (NACA) XX02 airfoil family using XFOIL. Subsequently, we employ a multi-objective optimization approach, utilizing a Class Shape Transformation (CST) airfoil parameterization to maximize lift and minimize drag. We select several points from the resulting Pareto front and evaluate their performance through unsteady compressible Navier-Stokes simulations. Our findings reveal that incorporating sharp leading-edge variations in these airfoil designs enhances peak efficiency by over 10%, primarily attributable to the development of Laminar Separation Bubbles (LSBs) on the suction side of the airfoils. Importantly, these modified airfoils maintain favorable performance at low angles of attack.

I. INTRODUCTION

The exploration of Mars has captured the interest of scientists and space agencies worldwide. Among the many challenges involved in designing aircraft and vehicles for Mars, the atmospheric conditions stand out. Mars has a much thinner atmosphere compared to Earth, with a surface pressure that is less than 1% of our planet's. This poses significant challenges in aerodynamic design for vehicles operating in this environment.

Numerous numerical and experimental studies have been conducted to address the design of airfoils specifically tailored for Martian atmospheric conditions. These studies primarily focus on the Ultra-low Reynolds number regime, which encompasses Reynolds numbers ranging from 1,000 to 10,000. Notably, Kunz[1] conducted one of the earliest comprehensive numerical investigations on efficient airfoils and rotors in these conditions. Similarly, Japanese researchers have made significant contributions to Martian flight research, providing extensive and valuable experimental data gathered from the Martian Wind Tunnel at Tohoku University[2–6]. These findings have served to validate various numerical approaches, spanning from commercial finite volume Navier-Stokes solvers[7,8] to high-order DNS (Direct Numerical Simulation) solvers[9]. However, it is worth noting that the primary focus of the Japanese researchers' efforts has been on analyzing airfoil performance under low Reynolds number conditions, specifically in the context of designing fixed-wing aircraft, as shown in several studies[3,10,11].

Regarding airfoil design for Martian rotors, Koning and coauthors[12,13] have presented detailed aerodynamic and optimization analyses of airfoils specifically for the Mars environment. Their study includes a multi-objective optimization aiming to simultaneously maximize lift and minimize drag. They concluded that airfoils with sharp leading-edge geometries exhibit higher peak aerodynamic efficiency compared to conventional geometries. This approach involves a computationally intensive process, as they incorporate URANS as a solver within their optimization loop. For the Mars Science Helicopter (MSH) developed within the Rotor Optimization for the Advancement of Mars eXploration (ROAMX) project[14], the authors selected a sharp double-edged plate as the airfoil[15]. Bézard and Desert[7,16–18] conducted extensive numerical and experimental research on airfoils for their coaxial helicopter design. They employed XFOIL[19] for the airfoil design, aiming to achieve globally optimal airfoils for various Reynolds numbers and angles of attack. In our work[20–22], we also contributed to the study of this regime. We presented the first set of numerical simulations resulting in different efficient Martian airfoil designs using a coupled Adjoint-based CFD analysis. To the best of the authors' knowledge, this represents the first application of such an approach to generate efficient airfoil designs for operation in the Martian atmosphere. Moreover, this methodology provides a computationally affordable means of including CFD simulations in the optimization procedure.

This work focuses on the behavior of airfoils operating at a Reynolds number of 10,000 and a Mach number of 0.5. In this particular regime, when the flow remains attached to the airfoil, it is considered subcritical. The Reynolds number in this range is consistently lower than the critical value required for the initiation of viscous instabilities or Tolmien-Schlitching waves that trigger the transition from laminar to turbulent flow. However, it is worth noting that even in subcritical flow, the transition to turbulence can still occur through different mechanisms. One such mechanism involves the initiation of an inviscid or Kelvin-Helmholtz instability, which causes the

Accepted to Phys. Fluids 10.1063/5.0166170

shear layer to roll up. As these vortical structures continue to evolve, they eventually become unstable and break down into smaller structures. This process is commonly referred to as separation-induced transition. Notably, in separation-induced transition, a significant amount of turbulent kinetic energy is produced in the separated shear layer, which promotes turbulent reattachment[23]. High-fidelity numerical simulations[24–26] have reproduced this transition mechanism for an SD7003 airfoil operating at a Reynolds number of 60,000 and an angle of attack of 4 degrees. These simulations reveal turbulent reattachment forming a separation bubble. However, when the same airfoil operates at a Reynolds number of 10,000, it exhibits laminar separation without transitioning to turbulence. Van Dyke[27] demonstrates the occurrence of leading-edge separation and posterior laminar reattachment without transitioning to turbulence for a flat plate operating at a Reynolds number of 10,000 and an angle of attack of 2.5 degrees. Pauley's research[28] concludes that the Kelvin-Helmholtz instability dominates laminar separation bubbles at low Reynolds numbers, with the transition to turbulence playing a secondary role. Carreño and D'Ambrosio[29] illustrate how the γ-Re$_\theta$ transition model accurately predicts transition at Reynolds 60,000 but becomes unreliable in the lower transitional regime. The activation of the turbulent term is observed to suppress vortex emission. Considering Pauley's findings, the limitations of transition models in this regime, and the computational cost of performing three-dimensional scale-resolving simulations in an optimization activity, we operate under the assumption of laminar flow. Koning[13] demonstrates good agreement between laminar and transitional simulations using an e^N model for a sharp leading-edge airfoil at moderate angles of attack, further supporting our assumption of laminar flow at Reynolds 10,000.

In this paper, we present a computationally efficient methodology that combines the speed of XFOIL for designing attached flow airfoils with a subsequent geometry modification to induce flow separation at the leading-edge. Initially, we evaluate the performance of two popular airfoil parametrizations: the National Advisory Committee for Aeronautics (NACA) and the Class Shape Transformation (CST) method. To further investigate the aerodynamic characteristics of airfoils in Martian atmospheric conditions, we compare the results obtained using XFOIL[19], a panel method with an integral boundary layer formulation, with those obtained using compressible Navier-Stokes solutions. This comparison offers insights into the accuracy of XFOIL in predicting aerodynamic performance in this regime. To optimize the airfoils' performance, we conduct a multi-objective optimization that simultaneously optimizes lift and drag using XFOIL. This optimization provides information on the trade-offs between lift and drag and the impact of different airfoil geometries on their performance. Finally, we examine the effects of incorporating sharp leading-edge versions of the optimal geometries on efficiency. We demonstrate how the peak efficiency can increase due to reduced skin friction and enhanced effective camber resulting from the formation of laminar separation bubbles.

II. METHODOLOGY AND THEORETICAL FRAMEWORK

A. Fitness function to optimize rotor performance

The most common and logical choice for the fitness function in airfoil optimizations is the lift-to-drag ratio, also known as aerodynamic efficiency[13,21]. However, some authors[17] argue that a combination of maximum aerodynamic efficiency and maximum range efficiency leads to less aggressive geometries. In the following analysis, we will demonstrate which value should be optimized based on the problem constraints for rotor optimization. The key parameter of interest in rotor optimization is the power loading, which can be defined as the ratio between the thrust generated and the power consumed by a rotor. Following the classical thrust and power definitions from the blade element theory[30], we can express this ratio as follows:

$$T/P = \frac{\int_{r_h}^{R}\left[(\Omega r)^2 + V_{ind}^2\right] c(r)\left[C_l(r)\cos(\phi) - C_d(r)\sin(\phi)\right] dr}{\int_{r_h}^{R}\Omega r\left[(\Omega r)^2 + V_{ind}^2\right] c(r)\left[C_d(r)\cos(\phi) + C_l(r)\sin(\phi)\right] dr} \tag{1}$$

In the previous expression, Ω is the rotation rate, V_{ind} is the induced velocity and $c(r)$ is the chord distribution along the span. The angle ϕ is the induced angle and will be defined in Eq. (7). The dependence on r, the radial coordinate, in the lift and drag coefficients indicates that we are considering a varying airfoil along the span. For a specific blade element located at position r, and simplifying the expression by omitting the dependencies on drag and lift coefficients for clarity, we can express it as follows:

$$\Delta(T/P) = \frac{C_l\cos(\phi) - C_d\sin(\phi)}{(\Omega r)\left[C_d\cos(\phi) + C_l\sin(\phi)\right]} \tag{2}$$

In this case, the radial station determines the incoming flow velocity, and the airfoil remains constant within the blade element. Assuming a uniform induction across an annular portion of the disk that corresponds to the blade element, the momentum theory[30] provides the following expression for the induction angle:

$$\phi = \arctan\left(\frac{V_{ind}}{\Omega r}\right) = \arctan\left(\frac{\sqrt{\dfrac{\Delta T}{4\rho\pi r\Delta r}}}{\Omega r}\right) \tag{3}$$

Using the Blade element theory and approximating for sufficiently small induction angles, we have:

$$\phi = \frac{\sqrt{\dfrac{0.5N_b\rho\left[(\Omega r)^2 + V_{ind}^2\right] c(r)\left[C_l\cos(\phi) - C_d\sin(\phi)\right]\Delta r}{4\rho\pi r\Delta r}}}{\Omega r} + O(\phi^3) \tag{4}$$

Due to its limited influence, we have neglected the tangential induction factor in Eq.3. Let's introduce the definition of local solidity:

$$\sigma_l = \frac{N_b c(r)}{2\pi r} \tag{5}$$

Accepted to Phys. Fluids 10.1063/5.0166170

where N_b is the number of blades. Using Eq. (5) and under the hypothesis of sufficiently small induction angles, so that

$$(\Omega r)^2 + V_{ind}^2 = (\Omega r)^2 \left(1 + \frac{V_{ind}^2}{(\Omega r)^2}\right) \approx (\Omega r)^2 \left(1 + \phi^2\right) \quad (6)$$

we can simplify Eq.3 to:

$$\phi = \sqrt{\frac{\sigma_l (1+\phi^2)\left[C_l \cos(\phi) - C_d \sin(\phi)\right]}{4}} \quad (7)$$

This equation is non-linear in ϕ and needs to be solved numerically. However, if we compare the two terms in the square brackets in Eq. 7, we note that:

$$\frac{C_d \sin(\phi)}{C_l \cos(\phi)} = \frac{\tan(\phi) C_d}{C_l} << 1 \quad (8)$$

so that:

$$\left[C_l \cos(\phi) - C_d \sin(\phi)\right] = C_l \cos(\phi)\left[1 - \frac{C_d \sin(\phi)}{C_l \cos(\phi)}\right] \simeq C_l \cos(\phi) \quad (9)$$

With the exception of radial stations close to the hub, where the aerodynamic efficiency is very low and significant induction angles are obtained, this approximation holds. In fact, an optimized airfoil at Reynolds 10,000 presents an efficiency of around 18, and induced angles are 10-15 degrees. Therefore, the errors will be contained within 1%.

Expanding $\cos(\phi)$ in Taylor series and rearranging Eq. 7, we obtain:

$$4\phi^2 = \sigma_l C_l (1+\phi^2)\left[1 - \frac{\phi^2}{2} + O(\phi^4)\right] = \sigma_l C_l \left[1 + \frac{\phi^2}{2} + O(\phi^4)\right] \quad (10)$$

Therefore:

$$\phi = \sqrt{\frac{2\sigma_l C_l}{8 - \sigma_l C_l}} \quad (11)$$

Equation 2 can be simplified according to Eq. 9 to obtain:

$$\Delta(T/P) = \frac{1}{\Omega r \left[\frac{C_d}{C_l} + \tan(\phi)\right]} \quad (12)$$

Next, we can expand $\tan(\phi)$ in Taylor series and make use of Eq. 11, so that

$$\Delta(T/P) = \frac{1}{\Omega r \left(\frac{C_d}{C_l} + \sqrt{\frac{2\sigma_l C_l}{8 - \sigma_l C_l}}\right)} \quad (13)$$

The expression in Eq. 13 demonstrates that, for a given rotation rate and radial station, the increasing aerodynamic effect positively influences power consumption. Additionally, minimizing the lift coefficient also has a beneficial impact due to reduced induced drag. However, it is important to compare T/P ratios only for equal thrusts. Therefore, one can establish a specific thrust level, ΔT_{req}, for a particular blade element, as follows:

$$\Delta T_{req} = \frac{1}{2}\rho \Omega^2 r^2 \sigma_l 2\pi \Delta r \left[C_l \left(1+\phi^2\right)\left(1 - \frac{\phi^2}{2}\right)\right] = \frac{1}{2}\rho \Omega^2 r^2 \sigma_l 2\pi \Delta r C_l \left(1 + \frac{\phi^2}{2}\right) \quad (14)$$

Given that we are at a specific radial station with a local thrust requirement, we can establish the following relationship between solidity, lift coefficient, and rotation rate:

$$\Omega^2 \sigma_l C_l \left(1 + \frac{\sigma_l C_l}{8 - \sigma_l C_l}\right) = K = K_2^2 = \frac{\Delta T_{req}}{\rho \pi r^3 \Delta r} \quad (15)$$

where K and K_2 are constants for a given density, thrust per unit length level, and radial station.

$$\Omega = \sqrt{\frac{K(r, \Delta T_{req}/\Delta r, \rho)}{\sigma_l C_l \left(1 + \frac{\sigma_l C_l}{8 - \sigma_l C_l}\right)}} = \frac{K_2(r, \Delta T_{req}/\Delta r, \rho)}{\sqrt{\sigma_l C_l \left(1 + \frac{\sigma_l C_l}{8 - \sigma_l C_l}\right)}} \quad (16)$$

$$\Delta(T/P) = \frac{1}{K_2(r, \Delta T_{req}/\Delta r, \rho)\left[\frac{1}{\sqrt{C_l \sigma_l \left(1 + \frac{\sigma_l C_l}{8 - \sigma_l C_l}\right)}} \frac{C_d}{C_l} + \frac{1}{2}\right]} \quad (17)$$

$$f = \sqrt{\sigma_l C_l \left(1 + \frac{\sigma_l C_l}{8 - \sigma_l C_l}\right)} \frac{C_l}{C_d} = \sqrt{\sigma_l \left(1 + \frac{\sigma_l C_l}{8 - \sigma_l C_l}\right)} \frac{C_l^{\frac{3}{2}}}{C_d} \quad (18)$$

The expression in Eq. 18 represents the objective function that should be maximized at each radial station. It is evident that by using the rotation rate as a design variable, the lift coefficient and solidity become more crucial, as they tend to increase the thrust coefficient. This result emphasizes the importance of achieving maximum aerodynamic efficiency in an optimal airfoil. However, to achieve the thrust restriction at a lower rotation rate and reduce power consumption, the airfoil must operate at a high lift coefficient.

Another significant factor that has been overlooked until now is the tip loss factor resulting from three-dimensional effects, which can be approximated by adjusting the local circulation. According to Kutta's formula, this adjustment is equivalent to modifying the lift coefficient using the Prandtl tip-loss correction formulated by Glauert[31]. In order to simplify the analysis and due to the weak dependence of the square root term on the lift coefficient, the correction will only be applied

to the lift coefficient outside the square root in Eq. 18.

$$f = \sqrt{\left(1+\frac{\sigma_l C_l}{8-\sigma_l C_l}\right)\sigma_l} \times \frac{\left\{C_l \frac{2}{\pi}\arccos\left[\exp\left(-\frac{N_b}{2}\frac{R-r}{r\sin\phi}\right)\right]\right\}^{\frac{3}{2}}}{C_d} = \frac{C_l}{C_d}\sqrt{\left(1+\frac{\sigma_l C_l}{8-\sigma_l C_l}\right)\sigma_l C_l} \times \left\{1-\frac{2}{\pi}\arcsin\left[\exp\left(-\frac{N_b}{2}\frac{R-r}{r\sqrt{\frac{2\sigma_l C_l}{8-\sigma_l C_l}}}\right)\right]\right\}^{\frac{3}{2}} \tag{19}$$

Performing further analytical comparisons becomes challenging at this point. However, it is important to note that the tip loss function will decrease as the lift coefficient increases. The extent of this decrease compared to the growth with the square root term will determine the actual function that needs to be optimized. To delve deeper into the analysis of this expression, let us divide the function into two parts:

$$f = \sqrt{\sigma_l} f_1 f_2 \tag{20}$$

with

$$f_1 = \sqrt{C_l\left(1+\frac{\sigma_l C_l}{8-\sigma_l C_l}\right)} \times \left\{1-\frac{2}{\pi}\arcsin\left[\exp\left(-\frac{N_b}{2}\frac{R-r}{r\sqrt{\frac{2\sigma_l C_l}{8-\sigma_l C_l}}}\right)\right]\right\}^{\frac{3}{2}} \tag{21}$$

and

$$f_2 = \frac{C_l}{C_d} \tag{22}$$

Figure 1 demonstrates the negligible impact of tip correction at the mid-span of the blade, where f_1 exhibits a square-root behavior. However, as we move towards higher radial stations, the slope of the curve decreases and becomes noticeably influenced by solidity. It is important to note that this analysis is an approximation as it does not consider the effects of Reynolds and Mach numbers. Despite these simplifications, it reveals that the objective function varies between aerodynamic efficiency $\frac{C_l}{C_d}$ and maximum range efficiency $\frac{C_l^{3/2}}{C_d}$ depending on the radial station and solidity. Thus, it is evident that aerodynamic efficiency alone is not sufficient for optimizing airfoils in rotor applications; instead, an optimal airfoil must exhibit maximum efficiency at a specific lift coefficient determined by the problem parameters. Consequently, a multi-objective optimization, considering both drag and lift coefficients as objectives, will yield a Pareto front of optimal airfoils for various rotor design conditions and radial stations. By analyzing the Pareto front in the $C_l - C_d$ plane, we can identify the points that correspond to $\frac{C_l}{C_d}$ and $\frac{C_l^{\frac{3}{2}}}{C_d}$ conditions

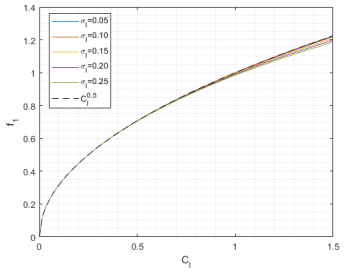

(a) r/R=0.5

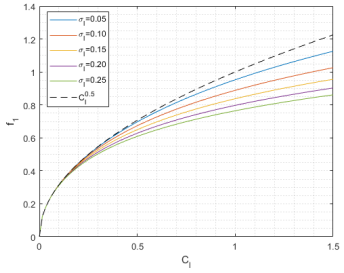

(b) r/R=0.75.

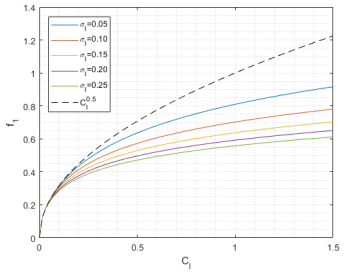

(c) r/R=0.85.

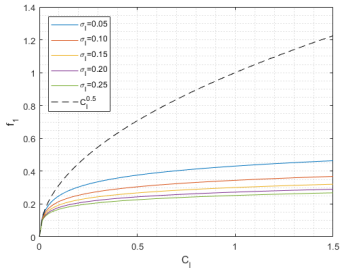

(d) r/R=0.95.

FIG. 1: f_1 function for different radial stations and solidities.

Accepted to Phys. Fluids 10.1063/5.0166170

by determining the slopes as given in Eqs. 23 and 24.

$$\max\left(\frac{C_l}{C_d}\right) \Longrightarrow \frac{d\left(\frac{C_l}{C_d}\right)}{dC_l} = \frac{C_d - C_l\frac{dC_d}{dC_l}}{C_d^2} = 0 \Longrightarrow \frac{dC_d}{dC_l} = \frac{C_d}{C_l} \tag{23}$$

$$\max\left(\frac{C_l^{\frac{3}{2}}}{C_d}\right) \Longrightarrow \frac{d\left(\frac{C_l^{\frac{3}{2}}}{C_d}\right)}{dC_l} = \frac{\frac{3}{2}C_l^{\frac{1}{2}}C_d - C_dC_l^{\frac{3}{2}}\frac{dC_d}{dC_l}}{C_d^2} = 0 \Longrightarrow \frac{dC_d}{dC_l} = \frac{3}{2}\frac{C_d}{C_l} \tag{24}$$

B. Airfoil Parametrizations

We consider two airfoil parametrizations in this study. Firstly, we utilize a classical NACA 4-digit formulation to conduct an initial exploration of the design space. Subsequently, we demonstrate how a more versatile CST parametrization can enhance the performance of the NACA series airfoils.

1. NACA 4-digits

The NACA airfoils are a specific category of aerodynamic airfoils that were studied and parameterized by the National Advisory Committee for Aeronautics. These airfoils are characterized by the digits that follow the acronym "NACA". The mathematical formulation of the NACA 4-digit airfoil is given by the following equations:

$$y_C = \tfrac{m}{p^2}(2px - x^2) \quad \text{for } 0 \le x \le p \tag{25a}$$

$$y_C = \tfrac{m}{(1-p)^2}[(1-2p) + 2px - x^2)] \quad \text{for } p \le x \le 1 \tag{25b}$$

$$y_t = \pm\frac{t}{0.2} \times (0.2969\sqrt{x} - 0.1260x - 0.3516x^2 + 0.2843x^3 - 0.1015x^4) \tag{25c}$$

where m represents the maximum camber, p denotes the location of the maximum camber, and t indicates the maximum thickness. All quantities are expressed as percentages of the chord length. In the NACA 4-digit notation, the first digit represents m multiplied by 100, the second digit represents p multiplied by 10, and the last two digits represent t multiplied by 100.

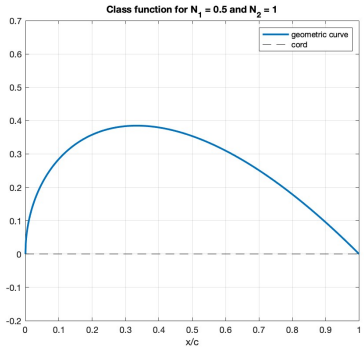

FIG. 2: Selected *class function* parameters for our CST.

To determine the upper and lower surface coordinates of the airfoil, the following transformations are applied:

$$x_U = x - y_t\sin\theta \tag{26a}$$
$$y_U = y_C - y_t\cos\theta \tag{26b}$$
$$x_L = x + y_t\sin\theta \tag{26c}$$
$$y_L = x_C - y_t\cos\theta \tag{26d}$$
$$\theta = \arctan\frac{dy_C}{dx} \tag{26e}$$

2. Class Shape Transformation (CST)

The CST parametrization can describe various geometric curves by utilizing a flexible number of degrees of freedom. The CST formulation, originally introduced by Kulfan and Bussoletti[32–34], is presented in Eq. 27. This approach involves employing two primary functions to recreate the desired shape: the *class function, C(x)*, and the *shape function, S(x)*.

$$\frac{y}{c} = C\left(\frac{x}{c}\right)S\left(\frac{x}{c}\right) + \frac{x}{c}\frac{\Delta z_{TE}}{c} \tag{27}$$

where, Δz_{TE}, represents the trailing edge thickness. The *class function* represents general categories of geometries, and its mathematical formulation is provided below:

$$C\left(\frac{x}{c}\right) = \left(\frac{x}{c}\right)^{N_1}\left(1-\frac{x}{c}\right)^{N_2} \quad ; \quad 0 \le \frac{x}{c} \le 1 \tag{28}$$

In our analysis, we have set $N_1 = 0.5$ and $N_2 = 1$ to achieve a round leading-edge and a sharp trailing edge, as illustrated in Figure 2.

The shape function serves as a form factor for the *class function*, and it is represented by a linear combination of the $n+1$ Bernstein polynomials of degree n, as defined in Eq. 29:

$$S\left(\frac{x}{c}\right) = \sum_{i=0}^{n} b_i\, B_{i,n} \tag{29}$$

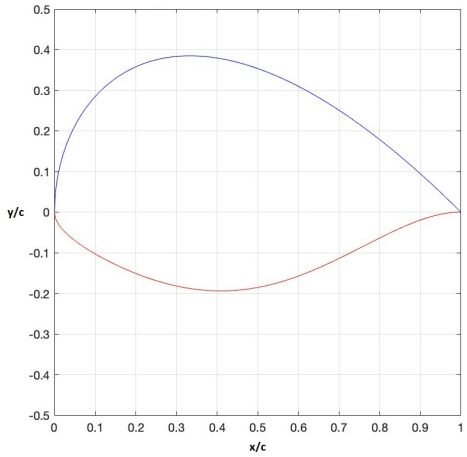

FIG. 3: Example of an airfoil generated with the CST parametrization.

The $n+1$ Berstein polynomials of degree n, $B_{i,n}$, are defined as shown in Eq. 30

$$B_{i,n} = \binom{n}{i}\left(\frac{x}{c}\right)^{i}\left(1-\frac{x}{c}\right)^{n-i} = \frac{n!}{i!\,(n-i)!}\left(\frac{x}{c}\right)^{i}\left(1-\frac{x}{c}\right)^{n-i} \quad ; \quad 0 \le x \le 1 \qquad i = 0,...,n \tag{30}$$

Figure 3 illustrates an example airfoil generated using our 8-parameter CST parametrization, which employs Bernstein polynomials of order 3 for both the upper and lower airfoil surfaces. The four parameters corresponding to the upper side are $[1,1,1,1]$ and the lower side of the airfoil is characterized by $[-0.3,-0.5,-0.8,0]$.

C. Numerical Methods

1. XFOIL

XFOIL[19] implements an algorithm that combines a potential flow panel method with an integral boundary layer formulation. Originally designed for estimating airfoil efficiency at low Reynolds numbers, XFOIL determines the pressure distribution and can account for laminar separation bubbles and mild trailing edge separation. In our study, we run XFOIL 6.99 from Matlab using the library provided by Edelman[35], which we modified to ensure the robustness of our optimization algorithm in the face of XFOIL failures or convergence issues.

To compute transition, XFOIL employs the estimated e^N envelope approach. This technique involves monitoring the most amplified frequency at a specific location downstream from the instability point on the airfoil to determine the disturbance magnitude. When the integrated amplitude exceeds an empirically defined threshold, transition is presumed and the boundary layer solver switches from laminar to turbulent. The appropriate value of N to be used in XFOIL computations can be determined using the following equation:

$$N = 8.43 - 2.4ln(Tu) \tag{31}$$

Here, Tu represents the freestream turbulence intensity. Uranga[25] demonstrates how XFOIL can predict separation-induced transition by properly tuning turbulence intensity. While XFOIL can reproduce the pressure plateau and subsequent recovery, it cannot predict the characteristic negative skin friction before reattachment. At our ultra-low Reynolds numbers, transition occurs only after boundary layer separation due to the amplification of Kelvin-Helmholtz instabilities. According to Pauley et al.[28], at very low Reynolds numbers, the primary cause of laminar separation bubbles is inviscid instability, with turbulence in the separated shear layer playing a secondary role. Consequently, we cannot expect XFOIL to adequately capture this phenomenon due to its steady nature. Therefore, our use of XFOIL is limited to attached flow conditions. To achieve this, we have set a very high value of the exponent N to prevent unphysical reattachment caused by flow transition, which would yield unrealistic airfoil efficiency values.

Figure 4 illustrates how XFOIL solutions with different Ncrit values collapse for low angles of attack. In these conditions, the flow remains attached, maintaining its laminar nature, and regardless of the chosen N value, the e^N criterion does not predict transition. At higher angles of attack, when using large Ncrit values, the flow separates while maintaining laminar flow, resulting in an increase in drag coefficient, while the lift coefficient remains relatively constant. Conversely, as Ncrit is decreased, the boundary layer reattaches due to the transition model triggering a transition to turbulent flow. This reattachment leads to an increase in lift and high-efficiency values. However, it's important to note that these values are highly dependent on the chosen Ncrit values. Therefore, using XFOIL in an optimization algorithm may produce airfoil geometries that induce transition instead of achieving efficient performance. To mitigate this, in our study, we run XFOIL with Ncrit set to 14 and disregard the lift and drag values obtained for angles of attack after flow separation.

It should be noted that XFOIL often fails to converge at high Mach numbers. To avoid discarding potentially good geometries solely due to convergence issues, we run XFOIL at low Mach numbers. Subsequently, we correct the pressure distributions using Kármán-Tsien's compressibility correction and integrate it to obtain lift and drag coefficients.

2. CFD

The two-dimensional compressible unsteady Navier-Stokes (NS) equations serve as the basis of the numerical model employed to calculate airfoil performance using the finite volume

Accepted to Phys. Fluids 10.1063/5.0166170

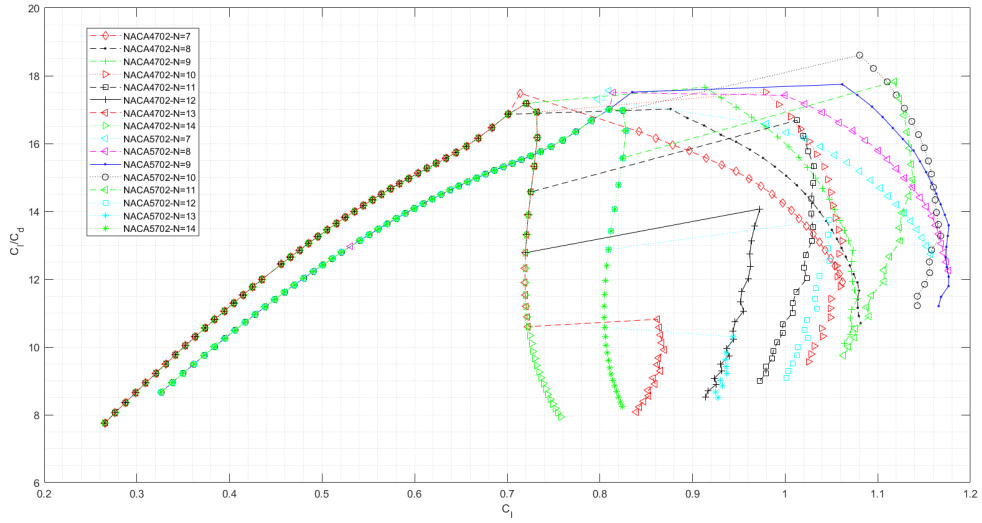

FIG. 4: Efficiency vs. lift coefficient for NACA 4702 and 5702 at Reynolds number of 10,000 using XFOIL with different N_{crit}.

solver embedded in STAR-CCM+. We consider a Newtonian fluid with constant dynamic viscosity. The freestream conditions are such that the Reynolds number based on the chord length is 10,000, and the Mach number is 0.5. Regarding spatial discretization, we use a third-order central difference scheme with a 15% upwind blending to enhance solution stability. A time step of 0.01 turnovers is employed, where a turnover is defined as c/U_∞, where c is the chord length and U_∞ is the freestream velocity. The simulations described in this study employ an implicit second-order dual time-stepping approach. The inner solver iterates 10 times per time step, reducing the residuals by 2-3 orders of magnitude. These settings ensure the resolution of the vortex shedding regime. Simulations are run for 100 turnovers to ensure statistical convergence. The airfoil performance data presented in this research is obtained by averaging unsteady loads over a sampling window of 20 turnovers.

Computational Domain

The computational domain adopted is depicted in Fig. 5, following the standards validated in Carreño et al. (2022)[29]. The domain extends approximately 1000 chords in the streamwise direction, with 400 chords upstream and 600 chords downstream. Crosswise, the domain spans 600 chords. This extensive domain size is chosen to mitigate the influence of far-field boundary conditions, as suggested for the NACA 0012 test case in the NASA Turbulence Modeling Resource[36]. Freestream inflow boundary conditions of Mach number, static pressure, and temperature are imposed

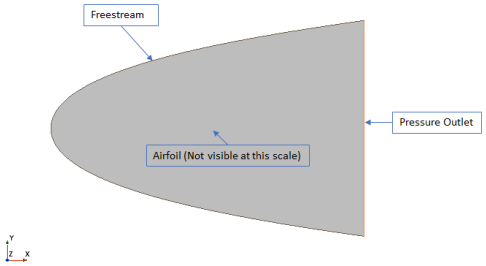

FIG. 5: Fluid domain and boundary conditions.

along a paraboloid-shaped surface. The freestream pressure is enforced on a flat "outflow" surface perpendicular to the freestream direction. The airfoil surface is treated as a non-slip, adiabatic wall.

Mesh

The computational grid incorporates polygonal cells and a near-wall prism layer to accurately capture the high gradients in the boundary layer and maintain mesh orthogonality near the body surface. In cases where boundary layer separation occurs at the leading-edge for certain angles of attack, the prism layer is confined to a thin zone near the wall, despite the low Reynolds number. Emphasizing wall-normal

TABLE I: Grid specifications.

Base size (m)	Target Chordwise spacing (%c)	Wake Refinement (%c)	Prism Layer Thickness (%c)
2	0.2	0.8	1
1	0.1	0.4	0.5
0.5	0.05	0.2	0.5

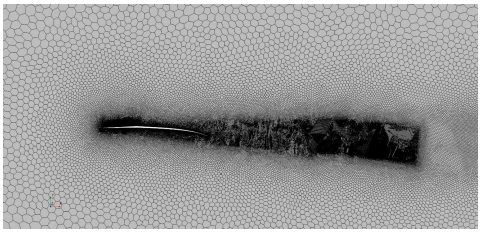

(a) Wake Refinement.

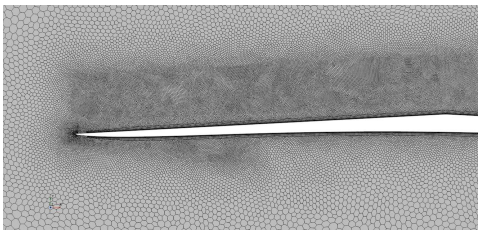

(b) Near-body detail.

FIG. 6: Mesh around Pareto Optimal airfoil at $C_l = 0.877$ with a sharp leading-edge obtained slicing with a 7.5 degrees plane, AOA=4.5°.

grid resolution in such scenarios would be futile since capturing strong gradients in all directions necessitates a well-refined mesh. Thus, we opt to limit the thickness of the prism layer by increasing the number of polygonal cells in the overlying area, where accurate resolution of the unsteady vortex-shedding structure is essential. To this end, a wake refinement is also included, as depicted in Fig. 6. The mesh contains 16 prism layers, with a near-wall distance that ensures a y+ value below 1. Table I provides the grid settings employed to construct three different meshes, demonstrating grid independence in the subsequent section. Figure 6 corresponds to the grid with a base size of 1 meter, which was selected for the 2D simulations presented in this paper. The base size serves as a reference length for scaling grid control settings and achieving uniform mesh refinement.

TABLE II: Grid Independence Study.

Base Size (m)	Cells	C_l	C_d
2	80,000	0.915	0.0471
1	200,000	0.945	0.0475
0.5	550,000	0.948	0.0477

TABLE III: Time-Step Independence Study.

Time-Step (Turnovers)	C_l	C_d
1/50	0.925	0.0470
1/100	0.945	0.0475
1/200	0.941	0.0474

Numerical convergence

Given the challenging flow characteristics, we conducted a convergence study to evaluate the spatial and temporal resolution for one of the sharp geometries considered in the following chapters. The results of this study are presented in Tables II and III. The grid and time-step settings outlined in the previous section were referred to a base size of 1 meter and a time-step of 0.01 turnovers. The airfoil chord length is 1 meter. It was found that reducing the resolutions by half resulted in variations of less than 0.5% in the results, indicating convergence in both time and space. The study was carried out on the airfoil discussed in Section IV, featuring a sharp leading-edge, with an angle of attack of 4.5 degrees, a Reynolds number of 10,000, and a Mach number of 0.5.

3. *Comparing XFOIL and CFD results*

In this section, we present a comparison between XFOIL and CFD results. The objective of this analysis is to demonstrate that XFOIL is capable of accurately predicting airfoil performance when the flow remains attached. Table IV compares the results at 4 degrees for NACA 4702 and NACA 5702, revealing differences below 5% between XFOIL and CFD. Figure 7 illustrate how the Kàrman-Tsien correction improves the incompressible prediction of the pressure coefficient on the airfoil's surface. The correction significantly enhances the prediction on the pressure side and most of the suction side, except for the suction peak, which is overestimated. This discrepancy may be attributed to the boundary

Accepted to Phys. Fluids 10.1063/5.0166170

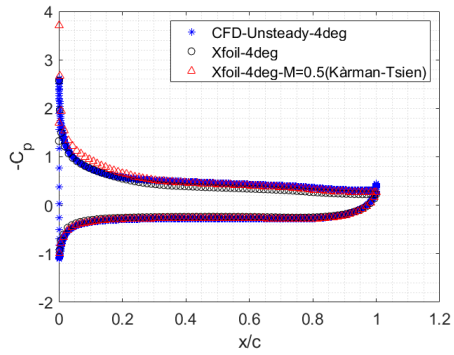

(a) Pressure coefficient for NACA-4702.

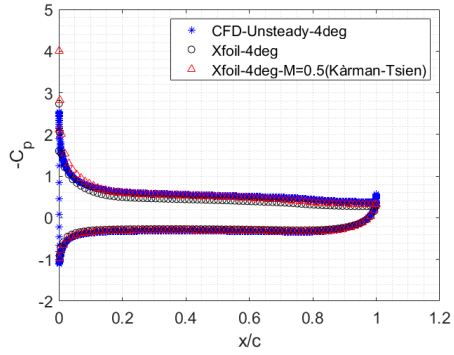

(b) Pressure coefficient for NACA-5702

FIG. 7: Pressure coefficient for NACA-4702 and NACA-5702 at Reynolds 10,000.

layer thickness being underestimated due to the omission of compressibility effects in the Von Kàrman equation solved by XFOIL. Nevertheless, it is evident that the overall integral loads are substantially improved with the incorporation of the correction.

Figure 8 demonstrate the close agreement between XFOIL and CFD in terms of lift and drag coefficients, as well as the resulting aerodynamic efficiency, particularly at low angles of attack. However, beyond the angle of attack where the maximum efficiency is achieved, XFOIL predicts a nearly constant lift with a noticeable increase in drag. In contrast, CFD predicts a high-lift regime due to the presence of low-pressure vortex cores emitted from the leading-edge. Although the drag also increases, the overall efficiency remains relatively high within a narrow range of angles of attack. Based on these findings, it is evident that XFOIL is capable of accurately capturing the attached flow regime. As a result, we will use XFOIL in the subsequent optimization exercise, which is presented in the following section.

III. AIRFOIL DESIGN AT REYNOLDS NUMBER OF 10,000

A. Analysis of a NACA 4-digits family

In this section, we calculate the performance of the entire NACA XX02 family using XFOIL to gain a comprehensive understanding of optimal camber and maximum camber positions. This information will be valuable for subsequent analysis. Following the development presented in Section II A, we have plotted both the aerodynamic and the maximum range efficiency, revealing that the optimal camber varies depending on the objective. Figure 9 demonstrates that cambers ranging from 3% to 5% are suitable for maximizing aerodynamic efficiency. Conversely, to maximize range efficiency, cambers between 5% and 7% are necessary. As for the maximum camber position, the optimal range lies between the 70% and the 80% of the chord for most cambers, with nearly identical performances. The upper envelope formed by all the curves corresponds to the airfoils found on the Pareto front in a multi-objective optimization using fitness functions C_l and C_d with the NACA XX02 family.

B. Multiobjective Genetic Optimization using XFOIL

We propose a Multi-Objective Optimization (MOO) approach utilizing a Genetic Algorithm (GA) with the CST airfoil parametrization, using lift and drag coefficients as objective functions. We adopt the MATLAB "gamultiobj" function, which is a variant of NSGA-II developed by Deb et al.[37], an elitist genetic algorithm. The population size is set to 300 individuals, and we select the top 35% of Pareto points that evolve over 100 generations. Table V provides the parameters and settings for the genetic algorithm. To enhance efficiency and convergence, we sweep angles of attack and identify the angle of attack that yields maximum efficiency. Although this choice limits the generality of our analysis, it is worth noting that selecting a high value for the N-factor parameter aligns the angle of attack of maximum efficiency closely with the incidence producing the highest lift coefficient. This alignment is influenced by XFOIL's inability to predict separated unsteady flows. Consequently, angles of attack beyond the maximum efficiency value would decrease efficiency while maintaining a constant lift, resulting in their exclusion from the Pareto front.

The Pareto front obtained in our multi-objective optimization has over 100 non-dominant airfoils. Figure 10 shows a selection of these airfoils obtained at different lift coefficients. Figure 11 shows the complete Pareto front. As we saw for the NACA series, the optimal camber increases with the target lift coefficient. Concerning the lower lift coefficients, the result is somehow unexpected, as we can see that the airfoils have a thick and rounded geometry near the leading-edge. That goes against the traditional design guidelines of ultra-low Reynolds

Accepted to Phys. Fluids 10.1063/5.0166170

TABLE IV: Airfoil performance predictions with XFOIL and CFD for two NACA airfoils at an angle of attack of 4 degrees. Reynolds number of 10,000 and Mach number of 0.5.

	C_l-NACA 4702	C_d-NACA 4702	C_l-NACA 5702	C_d-NACA 5702
XFOIL (Incompressible)	0.680	0.0414	0.733	0.0465
XFOIL (Kàrman-Tsien)	0.802	0.0480	0.862	0.0514
CFD	0.782	0.0466	0.877	0.0522

TABLE V: Genetic algorithm parameters.

Number of Variables	Population	Mutation	Cross-Over Rate	Pareto-set fraction	Generations
8	300	Adaptive Feasible	0.8	0.35	100

numbers airfoils. We believe that the genetic algorithm promotes these geometries to avoid leading-edge separation and hence the non-convergence of XFOIL. We use the Pareto front results to calculate the aerodynamic and maximum range efficiencies, shown in Fig. 12. We display the most performing airfoil for each efficiency metric in Fig. 12c. It is clear that they share genes regarding the leading-edge shape and thickness but with different maximum cambers. Figure 13 shows how, for lower lift coefficient values, the lower cambered geometry is more efficient using both metrics; however, the higher camber extends the efficiency window to higher lift coefficients. These trends are comparable to those observed for the NACA family.

Figure 16 shows the efficiencies of different airfoils calculated by unsteady compressible Navier-Stokes simulations at Reynolds 10,000 and Mach 0.5. The comparison includes the three most efficient airfoils from the NACA-XX02 family, three Pareto-optimal airfoils related to different lift coefficients (maximum aerodynamic efficiency, maximum range efficiency, and c_l=1.056), and the authors' optimized airfoil, PoliTO-2, designed via adjoint-based optimization[21]. The behavior of all airfoils before leading-edge separation is consistent with the results of XFOIL, as shown for the NACA airfoils in the previous section. In this situation, airfoils with smaller camber show improved efficiency at low angles of attack. The peak efficiency of the NACA airfoils is lower compared to the others. Interestingly, all Pareto-optimal airfoils have peak efficiencies around 18. However, we should distinguish between the first airfoils and the last with the highest lift coefficient. In the former cases, the peak efficiency is achieved with the flow attached, whereas in the latter case, the peak efficiency occurs after the leading-edge separation. The separated regime can be identified by the sudden increase in the lift coefficient between two consecutive angles of attack caused by the low-pressure cores of the vortices being shed above the suction side of the airfoil. For both NACA and Pareto-optimal airfoils, it is evident that higher camber gives better efficiency after leading-edge separation. The increased and delayed maximum camber position allows the large-scale vortices emitted at the leading edge to remain closer to the airfoil surface, as shown in Figure 14. The increase in efficiency is due to a narrower and thinner mean separation bubble, as shown in Figure 15.

In addition, the peak efficiencies reached by the airfoil optimized using the adjoint approach are comparable to those of the airfoils optimized using XFOIL. However, the range of efficient angles of attack is broader, indicating that the XFOIL approach can generate efficient geometries for attached flow conditions. Nevertheless, XFOIL cannot provide valuable information for the separated regime.

IV. SHARP LEADING-EDGE AIRFOILS

Recently, researchers from the ROAMX project decided to incorporate sharp, double-edged plate airfoils into the blades of the Mars Science Helicopter. These airfoil geometries have demonstrated superior performance to conventional shapes, with an increase in peak lift-to-drag ratio ranging from 17% to 41%[13]. The improved performance is related to the generation of large-scale vortex shedding caused by forced leading-edge separation, which has been extensively studied in the literature[7,16]. However, in several airfoils[7,21], the high-lift regime associated with low-pressure vortex cores on the suction side does not necessarily correlate with an increase in the lift-to-drag ratio.

We propose that the primary reason for the improved performance of sharp leading-edge airfoils lies in the characteristics of the mean laminar separation bubble. The pointed leading-edge generates a laminar separation bubble that can be either steady or unsteady depending on the Reynolds number and angle of attack. Such a separation bubble creates an effective curvature equivalent to a conventional airfoil but with reduced skin friction, resulting in a higher lift-to-drag ratio. However, the flow over a rotor with these sharp geometries is not yet fully understood. Spanwise pressure gradients and three-dimensional effects could introduce variations from the two-dimensional analysis performed to date. Regardless, a deeper understanding of the behavior of these sharp geometries is critical to realizing their potential.

In this section, we examine the sharp leading-edge variants of the airfoil with the maximum lift-to-drag ratio obtained pre-

Accepted to Phys. Fluids 10.1063/5.0166170

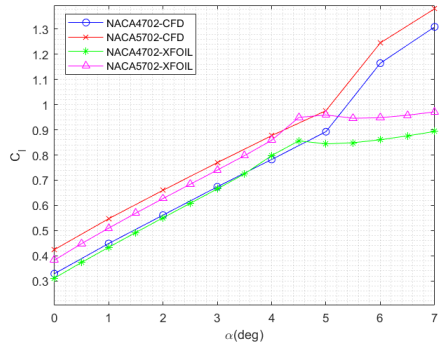

(a) Lift coefficient vs. angle of attack.

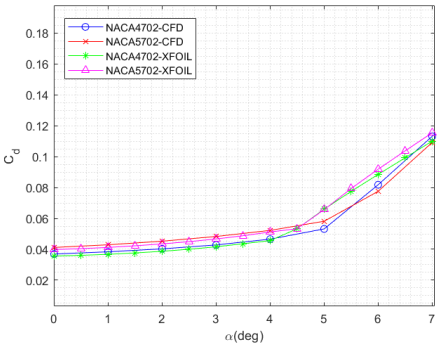

(b) Drag coefficient vs. angle of attack.

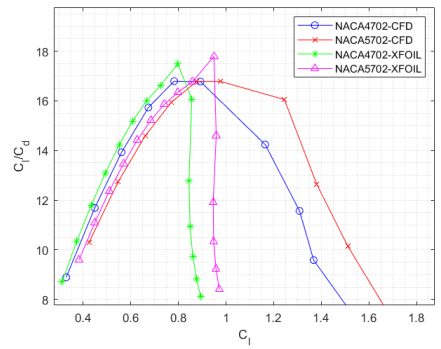

(c) Efficiency vs. lift coefficient.

FIG. 8: Aerodynamic coefficients for NACA 4-digit series airfoils at Re=10,000. XFOIL with N=14 vs CFD solver.

viously. The modified geometry is created by slicing the airfoil with planes inclined at various angles to the horizontal, as shown in Fig. 17. These airfoils combine the characteristics of sharp leading-edges and conventional airfoils. The underlying idea is that XFOIL produces highly efficient attached flow geometries. If it were possible to keep the external flow unchanged, the pressure distribution could remain the same while reducing skin friction. To this aim, the flat area on the suction side acts as a cavity for the separation bubble to stabilize and settle.

Figure 18 shows how the efficiency versus lift coefficient for sharp airfoils collapses with the rounded leading-edge geometry at low angles of attack. Such a collapse indicates that despite the presence of thick boundary layers, the efficiency of the airfoil is still predominantly influenced by the constant maximum camber, overshadowing any differences in local camber distributions. The sharp leading-edge versions of the Pareto-optimal geometry chosen for maximum range efficiency further support this behavior, as shown in Figure 19. Up to 3 degrees, for a given angle of attack, one can see that the lift coefficient slightly decreases as the cutting surface angle decreases. However, the aerodynamic efficiency remains insensitive to this parameter. This is interesting from a design perspective, as it suggests that airfoils can be optimized using a standard panel method approach that deals only with the attached flow and will subsequently improve its performance by transformation into sharp leading-edge versions when the flow separates. From 3 to 5 degrees, the lift coefficient is nearly identical for all airfoils. However, the efficiency is increased in sharp leading-edge airfoils, especially for the smallest slicing angles. This trend occurs because the separation bubble occupies a significant portion of the cavity, creating a local shear thrust that reduces the overall drag coefficient for the comparable lift coefficients. The drag reduction increases with the length of the flat section of the airfoil. This effect becomes more pronounced at higher angles of attack, where the mean separation bubble expands beyond the apex caused by the slicing. Figures 20–22 show the averaged velocity fields over 20 turnovers for different angles of attack, illustrating the evolution of the separation bubbles for the considered airfoils. It is clear that at 3 degrees the flow remains attached except for a small region near the leading edge where geometric separation occurs. As the angle of attack increases, a closed separation bubble is formed that reattaches in the vicinity of the apex. Finally, at 4.5 degrees the bubble occupies most of the suction side and reattaches well past the apex. Fig. 23 shows the instantaneous flow for the airfoil sliced with an angle of 7.5 degrees. At an angle of attack of 4 degrees, the bubble is anchored in the cavity created by the slicing and is confined to the region before the apex. The only unsteadiness detected is the beginning of a vortex shedding at the trailing edge. The anchorage of this bubble can be seen from the mean and instantaneous friction coefficients shown in Figure 24. They differ only at the trailing edge due to the vortex shedding, and they also show how the friction coefficient becomes positive before the apex, whose position is indicated by the sharp peak in the friction coefficient at about 30% of the chord. At 4.5 degrees, the separa-

Accepted to Phys. Fluids 10.1063/5.0166170

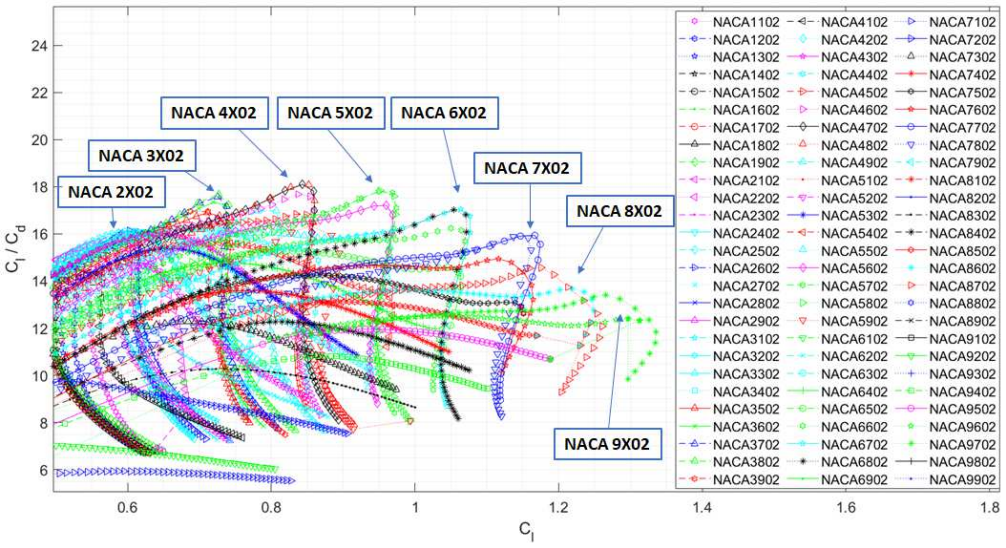

(a) Aerodynamic efficiency

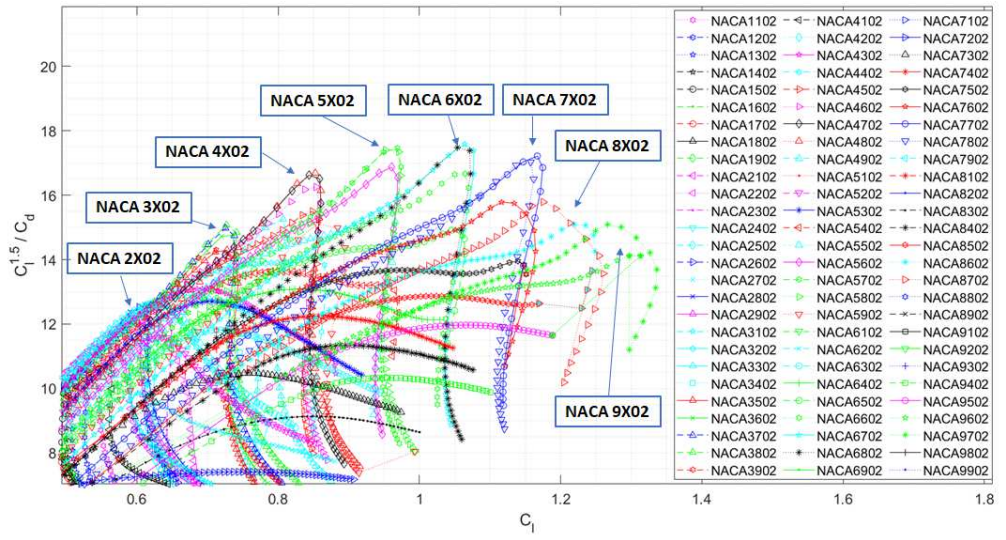

(b) Maximum range efficiency

FIG. 9: Efficiencies for the NACA-XX02 family airfoils at Reynolds 10,000 and Mach 0.5 using XFOIL with N=14.

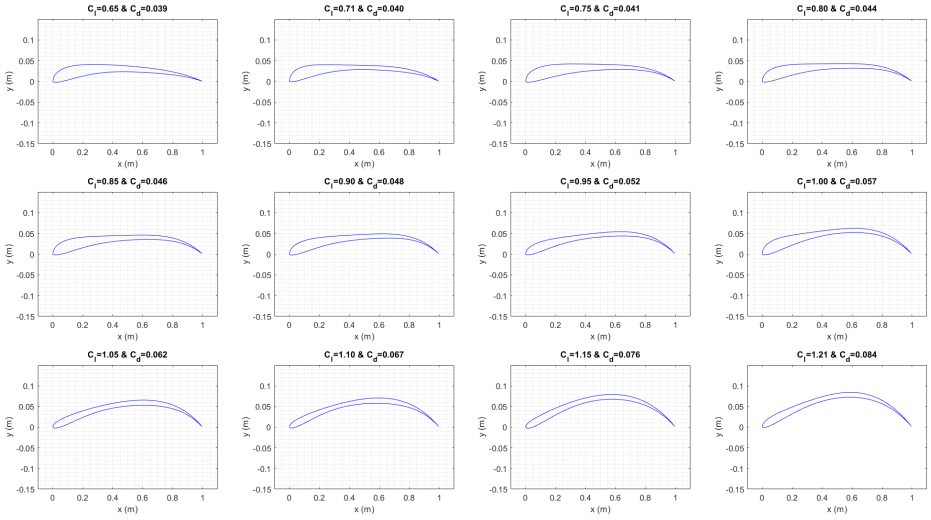

FIG. 10: A selection of Pareto optimal airfoil geometries for different lift coefficients.

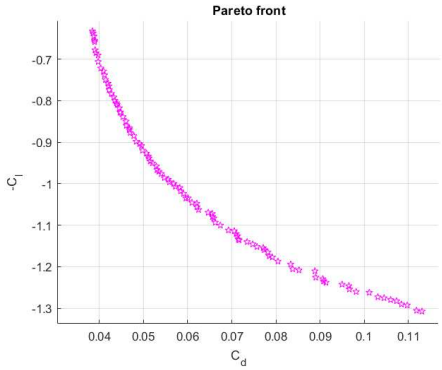

FIG. 11: Pareto front using the CST parametrization with XFOIL as a solver at Reynolds 10,000 and Mach 0.5.

tion bubble is too large to be confined before the apex, and a vortex is ejected from the apex and travels just above the surface of the airfoil, resulting in a high-lift regime due to the low-pressure vortex core remaining close to the suction side. The vortex emission can be clearly appreciated in Figure 25, which is characterized by strong oscillations in the instantaneous friction coefficient. It can also be seen how the mean separation bubble closes after the apex in this case. The increase in efficiency is related to the overall reduction in skin friction caused by the separation bubble on the suction side, which compensates for the increase in pressure drag due to the higher effective camber created by the separation bubble, as shown in Fig. 22. Table VI shows how slicing with a plane at 7.5 degrees produces a significant reduction in skin friction which is dominant compared to the increase in pressure drag. In addition, the aforementioned increase in effective camber causes a slight increase in the lift coefficient, resulting in an increase in the aerodynamic efficiency of the airfoil.

For slicing plane angles around 6.5 and 7.5 degrees, an optimal separation bubble appears that produces an effective camber for the external flow while maintaining a low level of skin friction. Drela[38] and Selig[39] investigated the concept of optimal separation bubbles for low Reynolds number airfoils and concluded that optimal separation bubbles are typically flat and short to prevent excessive increases in pressure drag while benefiting from reduced skin friction. However, their studies focused primarily on bubbles formed by the transition to turbulence in the separated shear layer, which increases the momentum near the wall. These bubbles often exhibit a "dead zone" with a near-zero coefficient of friction, as shown by Galbraith and Visbal[24] and Uranga, Persson, Drela, and Peraire[40] using the Implicit Large Eddy Simulations (ILES) at Reynolds numbers around 60,000. In our case, the bubbles arise from geometric separation at the leading-edge and exhibit laminar reattachment due to the development of the Kelvin-Helmholtz instability in the separated shear layer. Thus, the skin friction is negative and significantly strong, as shown in Fig. 25. Such a skin friction distribution leads to a negative viscous drag on the suction side. The fact that the shear stress contribution to the total drag is significant in the ultra-low Reynolds number regime further

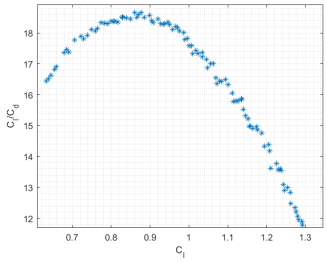

(a) Aerodynamic Efficiency.

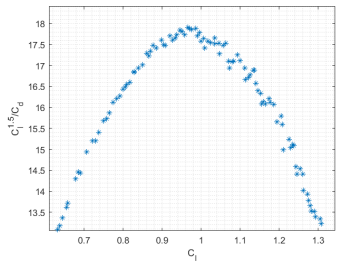

(b) Maximum Range Efficiency.

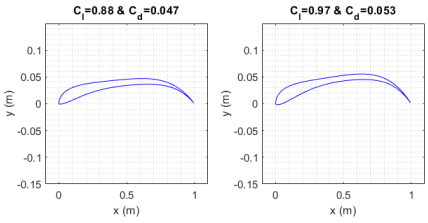

(c) Most performing airfoils in terms of aerodynamic (Left) and maximum range efficiency (Right).

FIG. 12: Efficiencies vs. lift coefficient for Pareto-optimal airfoils and most performing airfoils at Reynolds 10,000 using XFOIL with N=14.

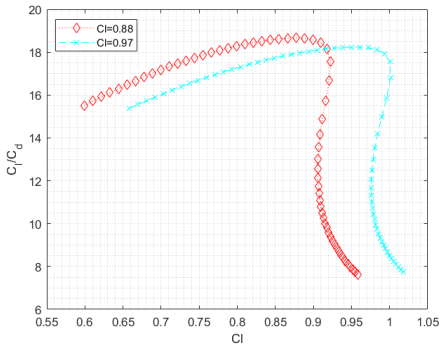

(a) Aerodynamic Efficiency.

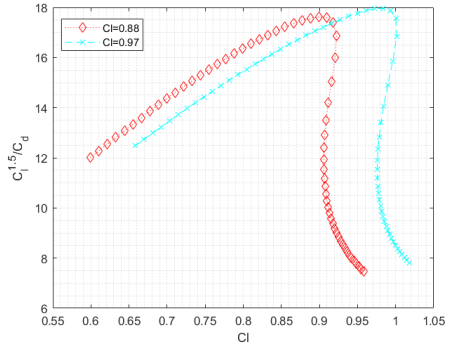

(b) Maximum Range Efficiency.

FIG. 13: Efficiency vs. lift coefficient for the two most performing Pareto-optimal airfoils at Reynolds 10,000 using XFOIL with N=14.

magnifies the positive effect of having a separation bubble on the suction side of the airfoil. In addition, the pressure distribution shown in Fig. 26 indicates high suction values due to the low pressure vortex cores.

The peak efficiency we found for both cases is about 20, exceeding the peak value of 18 observed in our previously proposed airfoil, PoliTO-2[21]. Our sharp airfoils have a slightly higher efficiency than the double-edged airfoil reported by Koning[13], which achieved a value of about 18 at Reynolds 10,117 and Mach 0.5 using unsteady Navier-Stokes simulations with the OVERFLOW solver. Bézard[7] showed that their airfoil reached a peak aerodynamic efficiency of about 15.5 under the same Mach and Reynolds number conditions, using unsteady Navier-Stokes simulations with the `elsa` solver. It is necessary to approach this comparison with caution, as these geometries are very sensitive to the numerical model used. Nevertheless, the results indicate that these airfoils, obtained at low computational cost, can achieve state-of-the-art performance levels.

TABLE VI: Impact of slicing in the aerodynamic performance of Pareto Optimal airfoil at $C_l = 0.877$. AOA=4.5º.

Airfoil	C_l	C_d**-Pressure**	C_d**-Friction**	C_d**-Total**
Standard	0.911	0.0311	0.0193	0.0504
Sliced 7.5º	0.945	0.0370	0.0105	0.0475
Difference (%)	+3.73	+18.97	-45.60	-5.75

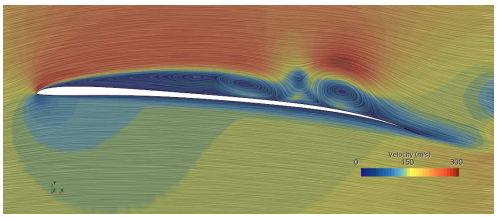

(a) $C_l = 0.877$.

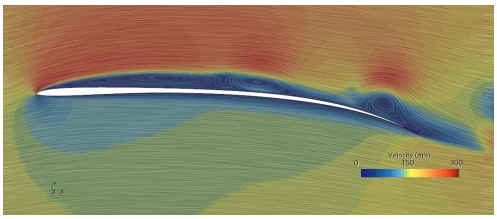

(b) $C_l = 1.056$.

FIG. 14: Instantaneous velocity field with streamlines on Pareto optimal airfoils. AOA=6º.

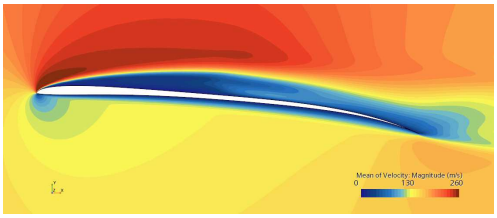

(a) $C_l = 0.877$.

(b) $C_l = 1.056$.

FIG. 15: Mean velocity field on Pareto optimal airfoils. AOA=6º.

V. CONCLUSIONS

This paper presents a numerical investigation of airfoil optimality at ultra-low Reynolds numbers. Assuming laminar flow, we perform various analyses using XFOIL and compressible Navier-Stokes simulations. Our results show that XFOIL and CFD predictions are comparable when the flow remains attached, but XFOIL predicts airfoil stall when the flow separates. Conversely, CFD simulations predict a high lift regime associated with low-pressure vortex cores emanating from the leading-edge and traveling downstream near the suction side of the airfoil.

We begin with a preliminary exploration of the design space using the NACA XX02 family. We show that for attached flow conditions, the optimal camber for maximizing aerodynamic efficiency is between 3% and 5%. Conversely, for maximum range efficiency, slightly larger cambers between 4% and 6% are required. The optimal value for camber position is determined to be equally effective in a range between 70% and 80% of chord. Our multi-objective optimization aligns with these results, yielding an airfoil with 4% camber to maximize aerodynamic efficiency and an airfoil with 5% camber to optimize maximum range efficiency. In addition, multi-objective optimization produces a range of optimal airfoils for different lift coefficients. This is a crucial aspect as we show that using a constant fitness function to optimize airfoils at different radial coordinates is insufficient to achieve globally optimal designs, especially in rotor applications.

In terms of airfoil performance after leading-edge separation, we observe that airfoils with smaller cambers exhibit degraded performance because the large-scale vortices emitted by the leading-edge travel farther away from the airfoil surface than those with higher cambers. Consequently, higher-camber airfoils have a wider operating window of high efficiency, despite a slight reduction in peak efficiency.

Finally, we show how sharp geometries derived from the previously optimized airfoils improve peak performance by approximately 10%. This improvement occurs over a narrow range of angles of attack, approximately 2 degrees. However, we show that the proposed slicing method does not affect the aerodynamic efficiency at lower angles of attack. Therefore, for a given lift coefficient, sharp geometries perform at least as well as rounded leading-edge geometries, except at large angles of attack. The improved efficiency is due to the presence of separation bubbles on the suction side of the airfoil, which introduce slightly more camber while significantly reducing shear drag. Optimal separation bubbles at ultra-low Reynolds numbers are more elongated than those at higher Reynolds numbers. In fact, these bubbles generate intense negative shear stress, resulting in a thrust component that reduces the overall shear stress and extends the dimensions of the optimal bubbles beyond those found at higher Reynolds numbers.

DATA AVAILABILITY STATEMENT

The data that support the findings of this study are available from the corresponding author upon reasonable request.

Accepted to Phys. Fluids 10.1063/5.0166170

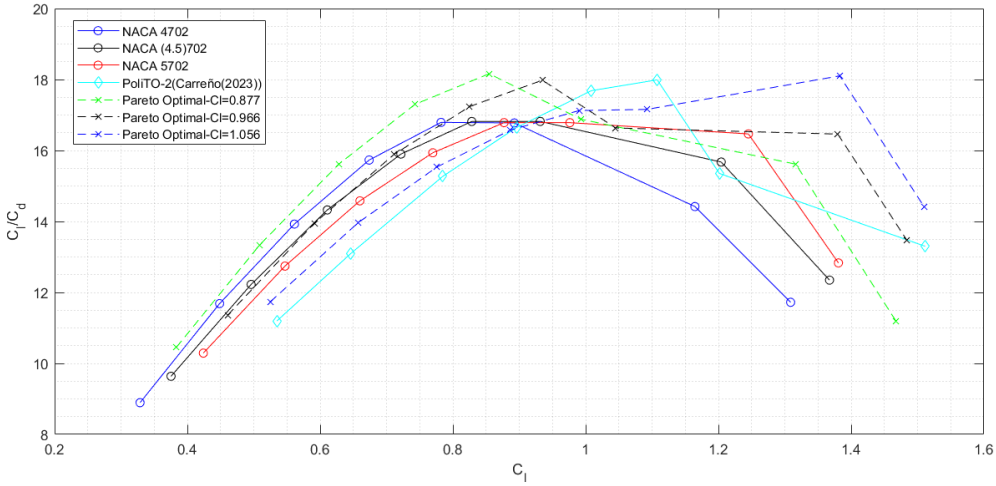

FIG. 16: Efficiency vs. lift coefficient for three Pareto-optimal airfoils, three most performing NACA-xx02 family airfoils, and an adjoint-optimized airfoil at Reynolds 10,000 and Mach 0.5. Results were obtained using compressible unsteady Navier-Stokes simulations.

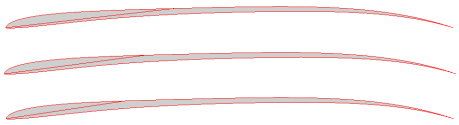

FIG. 17: Sharp leading-edge geometry. 6.5^o (top), 7.5^o (middle) and 8.5^o (bottom).

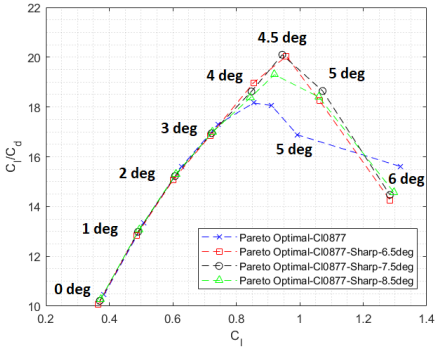

FIG. 18: Efficiency vs. lift coefficient for Pareto optimal airfoils with and without sharp leading-edges.

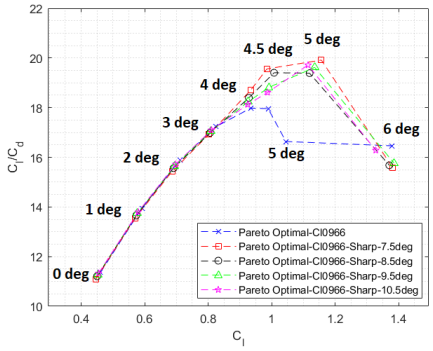

FIG. 19: Efficiency vs. lift coefficient for Pareto optimal airfoils with and without sharp leading-edges.

REFERENCES

[1]P. J. Kunz, *Aerodynamics and design for ultra-low Reynolds number flight*, Ph.D. thesis, Standford University (2003).
[2]P. M. Munday, K. Taira, T. Suwa, D. Numata, and K. Asai, "Nonlinear lift on a triangular airfoil in low-Reynolds-number compressible flow," Journal of Aircraft **52**, 924–931 (2015).
[3]M. Anyoji, T. Nonomura, H. Aono, A. Oyama, K. Fujii, H. Nagai, and K. Asai, "Computational and Experimental Analysis of a High-

Accepted to Phys. Fluids 10.1063/5.0166170

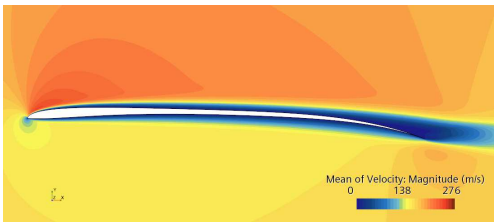

(a) Pareto Optimal Geometry $C_l = 0.877$.

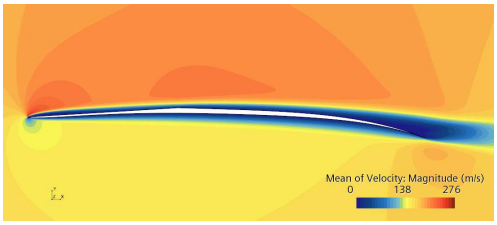

(b) Pareto Optimal Geometry $C_l = 0.877$. Sliced with plane at 6.5º

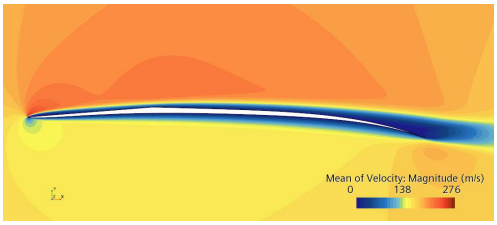

(c) Pareto Optimal Geometry $C_l = 0.877$. Sliced with plane at 7.5º

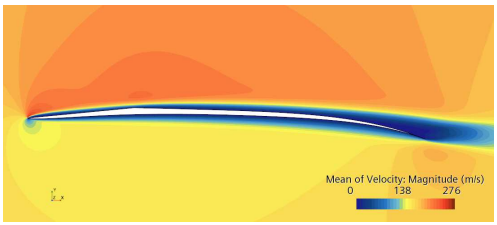

(d) Pareto Optimal Geometry $C_l = 0.877$. Sliced with plane at 8.5º

FIG. 20: Mean velocity field around sharp and round versions of maximum efficiency airfoil, AOA=3°.

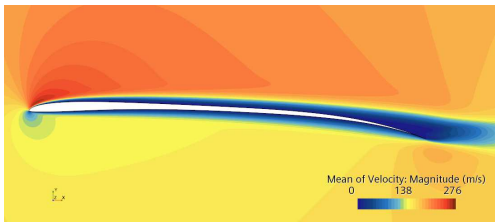

(a) Pareto Optimal Geometry $C_l = 0.877$.

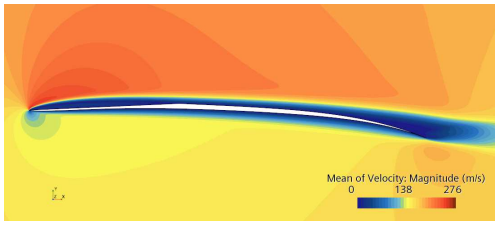

(b) Pareto Optimal Geometry $C_l = 0.877$. Sliced with plane at 6.5º

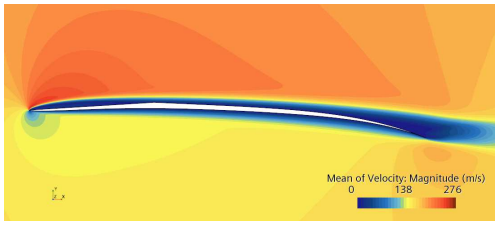

(c) Pareto Optimal Geometry $C_l = 0.877$. Sliced with plane at 7.5º

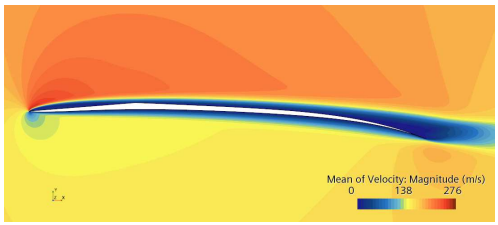

(d) Pareto Optimal Geometry $C_l = 0.877$. Sliced with plane at 8.5º

FIG. 21: Mean velocity field around sharp and round versions of maximum efficiency airfoil, AOA=4°.

Performance Airfoil Under Low-Reynolds-Number Flow Condition," Journal of Aircraft **51**, 1864–1872 (2014).
[4]T. Suwa, K. Nose, D. Numata, H. Nagai, and K. Asai, "Compressibility Effects on Airfoil Aerodynamics at Low Reynolds Number," (AIAA, New Orleans, LA, June 25-28, 2012) AIAA-2012-3029.
[5]M. Anyoji, H. Nagai, and K. Asai, "Development of low density wind tunnel to simulate atmospheric flight on Mars," in *47th AIAA Aerospace Sciences Meeting including The New Horizons Forum and Aerospace Exposition* (Orlando, FL, January 2009) AIAA-2009-1517.
[6]M. Anyoji, K. Nose, S. Ida, D. Numata, H. Nagai, and K. Asai, "Low Reynolds Number Airfoil Testing in a Mars Wind Tunnel," (AIAA, Chicago, IL, Jun. 28 – Jul. 1, 2010) AIAA 2010-4627.
[7]H. Bézard, T. Desert, J.-M. Moschetta, and T. Jardin, "Aerodynamic design of a Martian micro air vehicle," in *EUCASS 2019* (MADRID, Spain, 2019).
[8]M. Carreño Ruiz and D. D'Ambrosio, "Validation and application of aerodynamic simulations in the Martian atmosphere," in *26th Conference of the Italian Association of Aeronautics and Astronautics-AIDAA 2021* (2021).
[9]L. Caros, O. Buxton, T. Shigeta, T. Nagata, T. Nonomura, K. Asai, and P. Vincent, "Direct Numerical Simulation of Flow over a Triangular Airfoil Under Martian Conditions," AIAA Journal **60**, 3961–3972 (2022).
[10]M. Anyoji and D. Hamada, "High-Performance Airfoil with Low Reynolds-Number Dependence on Aerodynamic Characteristics," Fluid Mechanics

(a) Pareto Optimal Geometry $C_l = 0.877$.

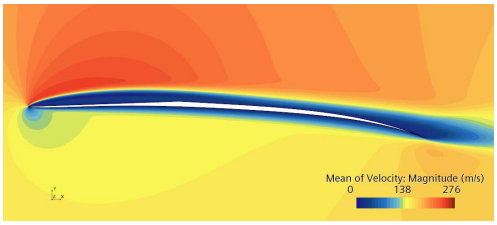

(b) Pareto Optimal Geometry $C_l = 0.877$. Sliced with plane at 6.5º

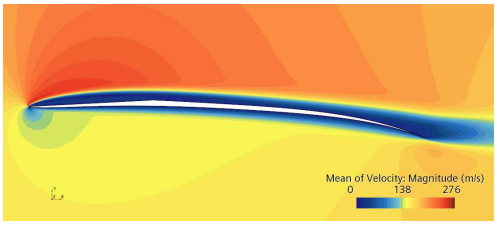

(c) Pareto Optimal Geometry $C_l = 0.877$. Sliced with plane at 7.5º

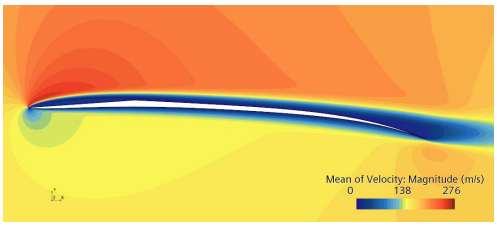

(d) Pareto Optimal Geometry C_l=0.877. Sliced with plane at 8.5º

FIG. 22: Mean velocity field around sharp and round versions of maximum efficiency airfoil, AOA=4.5°.

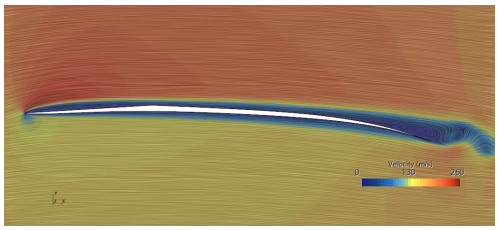

(a) AOA=4.0°.

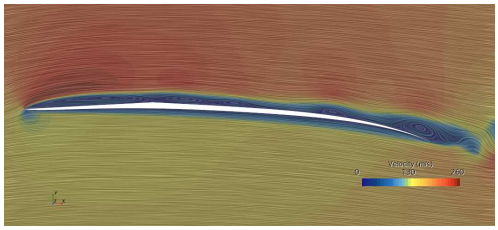

(b) AOA=4.5°.

FIG. 23: Instantaneous velocity field around the sharp versions of maximum efficiency airfoil, with a slicing plane of 7.5 degrees.

Research International Journal **3**, 76–80 (2019).

[11] H. Aono, M. Anyoji, D. Hamada, S. Wakui, and T. Tatsukawa, "A Study on Development of Airfoil Shape Toward Low Reynolds-Number Dependence of Aerodynamic Characteristics Under Low-Reynolds-Number-Flow conditions," in *2018 AIAA Aerospace Sciences Meeting* (Kissimmee, FL, 8-12 January 2018) AIAA-2018-1085.

[12] W. J. Koning, W. Johnson, and B. G. Allan, "Generation of Mars Helicopter Rotor Model for Comprehensive Analyses," AHS Aeromechanics Design for Transformative Vertical Flight (2018).

[13] W. J. Koning, E. A. Romander, and W. Johnson, "Optimization of Low Reynolds Number Airfoils for Martian Rotor Applications Using an Evolutionary Algorithm," in *AIAA SciTech 2020 Forum* (Orlando, FL, January 2020) AIAA-2020-0084.

[14] H. Cummings, B. N. P. Perez, W. Koning, W. Johnson, L. Young, F. Haddad, E. Romander, J. Balaram, T. Tzanetos, J. Bowman, *et al.*, "Overview and Introduction of the Rotor Optimization for the Advancement of Mars eXploration (ROAMX) Project," in *Aeromechanics for Advanced Vertical Flight Technical Meeting, Transformative Vertical Flight 2022* (2022).

[15] W. Johnson *et al.*, "Mars science helicopter conceptual design," NASA/TM—2020–220485 (March 2020).

[16] H. Bézard, T. Désert, T. Jardin, and J.-M. Moschetta, "Numerical And Experimental Aerodynamic Investigation Of A Micro-UAV For Flying On Mars," in *76th Annual Forum & Technology Display* (Virginia Beach, VA, october 2020) hal-02901622.

[17] T. Desert, J.-M. Moschetta, and H. Bézard, "Numerical and experimental investigation of an airfoil design for a Martian micro rotorcraft," International Journal of Micro Air Vehicles **10**, 262–272 (2018).

[18] T. Désert, T. Jardin, H. Bézard, and J.-M. Moschetta, "Numerical predictions of low Reynolds number compressible aerodynamics," Aerospace Science and Technology **92**, 211–223 (2019).

[19] M. Drela, "XFOIL: An analysis and design system for low Reynolds number airfoils," in *Low Reynolds number aerodynamics* (Springer, 1989) pp. 1–12.

[20] M. Carreño Ruiz and D. D'Ambrosio, "Aerodynamic Optimization of Quadrotor Blades Operating in the Martian Atmosphere," in *AIAA SciTech 2022 Forum* (San Diego, CA, January 2022) AIAA-2022-0743.

[21] M. Carreño Ruiz and D. D'Ambrosio, "Aerodynamic optimization and analysis of quadrotor blades operating in the Martian atmosphere," Aerospace Science and Technology **132**, 108047 (2023).

[22] M. Carreño Ruiz and D. D'Ambrosio, "Hybrid Fidelity Optimization of Efficient Airfoils and Rotors in Ultra-Low Reynolds Numbers Conditions," in *AIAA SciTech 2023 Forum* (National Harbor, MD, January 2023) AIAA-2023-0652.

[23] R. B. Langtry and F. R. Menter, "Correlation-based transition modeling for unstructured parallelized computational fluid dynamics codes," AIAA journal **47**, 2894–2906 (2009).

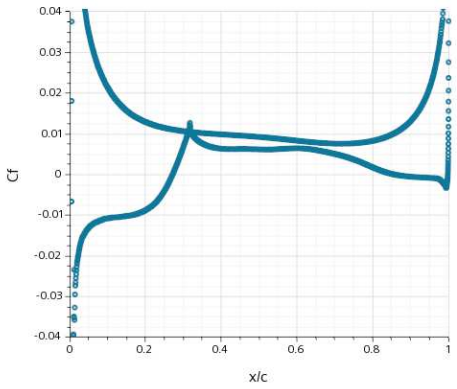

(a) Instantaneous Friction Coefficient.

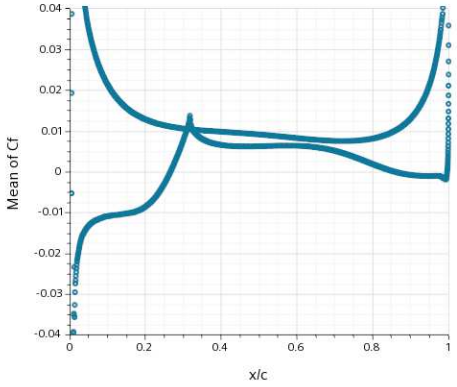

(b) Time-Averaged Friction Coefficient

FIG. 24: Friction Coefficient for Pareto Optimal Airfoil at $C_l = 0.877$. Sliced with a plane at 7.5°, AOA=4.0°.

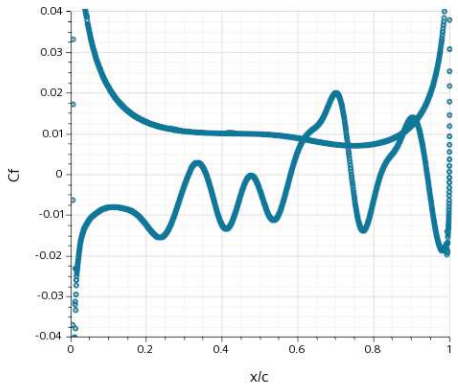

(a) Instantaneous Friction Coefficient.

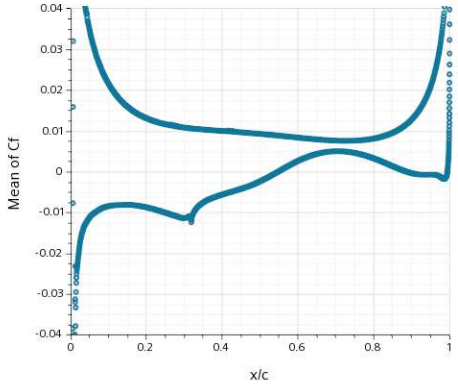

(b) Time-Averaged Friction Coefficient

FIG. 25: Friction Coefficient for Pareto Optimal Airfoil at $C_l = 0.877$. Sliced with a plane at 7.5°, AOA=4.5°.

[24]M. Galbraith and M. Visbal, "Implicit large eddy simulation of low-Reynolds-number transitional flow past the SD7003 airfoil," in *40th Fluid Dynamics Conference and Exhibit*, edited by AIAA (Chicago, IL, 28 June – 1 July 2010) AIAA 2010-4737.
[25]A. Uranga, *Investigation of transition to turbulence at low Reynolds numbers using Implicit Large Eddy Simulations with a Discontinuous Galerkin method*, Ph.D. thesis, University of California, Berkeley (2010).
[26]C. Carton de Wiart and K. Hillewaert, "DNS and ILES of transitional flows around a SD7003 using a high order Discontinuous Galerkin Method," in *Seventh International Conference on Computational Fluid Dynamics (ICCFD7)* (Big Island, HI, July 9-13, 2012) iCCFD7–3604.
[27]M. Van Dyke, *An Album of Fluid Motion* (The Parabolic Press, Stanford, 1982).
[28]L. L. Pauley, P. Moin, and W. C. Reynolds, "The structure of two-dimensional separation," Journal of Fluid Mechanics **220**, 397–411 (1990).
[29]M. Carreño Ruiz and D. D'Ambrosio, "Validation of the $\gamma - Re_\theta$ Transition Model for Airfoils Operating in the Very Low Reynolds Number Regime," Flow, Turbulence and Combustion **109**, 279–308 (2022).
[30]G. J. Leishman, *Principles of helicopter aerodynamics* (Cambridge university press, 2006).
[31]H. Glauert, "The effect of compressibility on the lift of an aerofoil," Proceedings of the Royal Society of London. Series A, Containing Papers of a Mathematical and Physical Character **118**, 113–119 (1928).
[32]B. M. Kulfan and J. E. Bussoletti, ""Fundamental" Parametric Geometry Representations for Aircraft Component Shapes," in *11th AIAA/ISSMO Multidisciplinary Analysis and Optimization Conference* (Portsmouth, VA, 6-8 September, 2006) AIAA-2006-6948.
[33]B. M. Kulfan, "Recent extensions and applications of the 'CST' universal parametric geometry representation method," The Aeronautical Journal **114**, 157–176 (2010).
[34]M. Ceze, M. Hayashi, and E. Volpe, "A study of the CST parameterization characteristics," in *27th AIAA Applied Aerodynamics Conference* (San Antonio, TX, 22-25 June, 2009) AIAA-2009-3767.
[35]L. Edelman, "Xfoil interface updated," (2014), accessed: June 26, 2023.

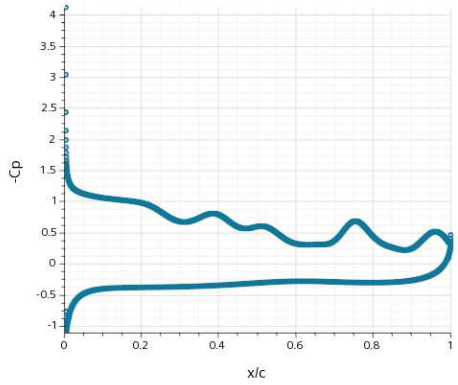

(a) Instantaneous Pressure Coefficient.

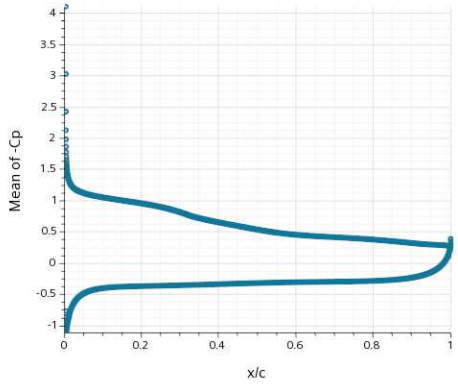

(b) Time-Averaged Pressure Coefficient

FIG. 26: Pressure Coefficient for Pareto Optimal Airfoil at $C_l = 0.877$. Sliced with a plane at 7.5º, AOA=4.5°.

[36] C. Rumsey, "Langley Research Center. Turbulence Modeling Resource. 2D NACA 0012 airfoil validation case. Effect of farfield boundary," (2014), accessed: June 24, 2022.
[37] K. Deb, "Multi-objective optimisation using evolutionary algorithms: an introduction," in *Multi-objective evolutionary optimisation for product design and manufacturing* (Springer, 2011) pp. 3–34.
[38] M. Drela, "Low-Reynolds-number airfoil design for the MIT Daedalus prototype-A case study," Journal of Aircraft **25**, 724–732 (1988).
[39] M. Selig, "Low Reynolds number airfoil design lecture notes," VKI Lecture Series , 1–43 (24-28 November, 2003).
[40] A. Uranga, P.-O. Persson, M. Drela, and J. Peraire, "Implicit Large Eddy Simulation of Transitional Flows Over Airfoils and Wings," in *19th AIAA Computational Fluid Dynamics* (2009) AIAA-2009-4131.